Current Optics and Photonics
Vol. 5, No. 6, December 2021, pp. 672–679

ISSN: 2508-7266(Print) / ISSN: 2508-7274(Online)
DOI: https://doi.org/10.3807/COPP.2021.5.6.672

Parallel Synthesis Algorithm for Layer-based Computer-generated Holograms Using Sparse-field Localization

Jongha Park[1], Joonku Hahn[2], and Hwi Kim[1]*

[1]*Department of Electronics and Information Engineering, Korea University, Sejong 30019, Korea*
[2]*School of Electronics Engineering, Kyungpook National University, Daegu 41566, Korea*

(Received June 17, 2021 : revised July 27, 2021 : accepted August 31, 2021)

We propose a high-speed layer-based algorithm for synthesizing computer-generated holograms (CGHs), featuring sparsity-based image segmentation and computational parallelism. The sparsity-based image segmentation of layer-based three-dimensional scenes leads to considerable improvement in the efficiency of CGH computation. The efficiency enhancement of the proposed algorithm is ascribed to the field localization of the fast Fourier transform (FFT), and the consequent reduction of FFT computational complexity.

Keywords : Diffractive optics, Digital holography, Fast algorithms, Localization
OCIS codes : (090.0090) Holography; (090.1760) Computer holography; (090.1970) Diffractive optics; (090.1995) Digital holography

I. INTRODUCTION

In recent years, finding fast algorithms for creating computer-generated holograms (CGHs) has been a central issue in the development of holographic three-dimensional (3D) display technology. A variety of algorithms have emerged to address the practical issues of CGH computation, such as computational efficiency, holographic-image quality, and object-modeling methods [1, 2]. The main CGH algorithms can be categorized according to method as point-cloud [3], layer-based (depth-map) [4, 5], light-field [6], polygon [7, 8], and wave-recording plane CGH synthesis methods and their variations [9]. Of these algorithms, the layer-based CGH synthesis method is considered to have attained sufficient CGH image quality and computational efficiency for practical application. Its efficiency is achieved by the approximation made when modeling a layer 3D scene, as shown in Fig. 1. Figures 1(a) and 1(b) present a color-depth-map image featuring 256 depth levels. Each depth layer contains sparsely sliced image information. For example, Fig. 1(c) shows the slice of the image at the 200$^{\text{th}}$ depth plane. It can be seen that the range occupied by nonzero data in a single depth plane is quite sparse. This sparsity means that the majority of the depth plane is zero-valued, and only a comparatively small part of the depth plane is nonzero-valued. Therefore, it is possible to reduce the computational area by allocating the region of interest (ROI) as shown in Fig. 1(d).

The depth-layer model allows us to use the fast Fourier transform (FFT) between the depth plane and the spatial light modulator (SLM). The full-size 3D scene projection image is divided and distributed into different depth layers, as seen in Fig. 1(e). To construct the single full-size complex CGH pattern, all slices of a 3D scene should be back-propagated into the SLM plane. The conventional calculation scheme for layer-based CGH is schematically depicted in Fig. 1(e), including the eye of the viewer, and consisting of an eye-lens plane, a retinal plane, and an SLM plane.

The image of a depth layer L_m is given in the retina plane with the eye's focus adjusted to the layer in the object space, and the image field of the retina plane backwardly transformed to the SLM plane forming a partial CGH, which is referred to as the m^{th} partial component of the total CGH pattern. This process is referred to as the inverse cascaded Fresnel transform (ICdFr) [5], and the layered 3D

*Corresponding author: hwikim@korea.ac.kr, ORCID 0000-0002-4283-8982

Color versions of one or more of the figures in this paper are available online.

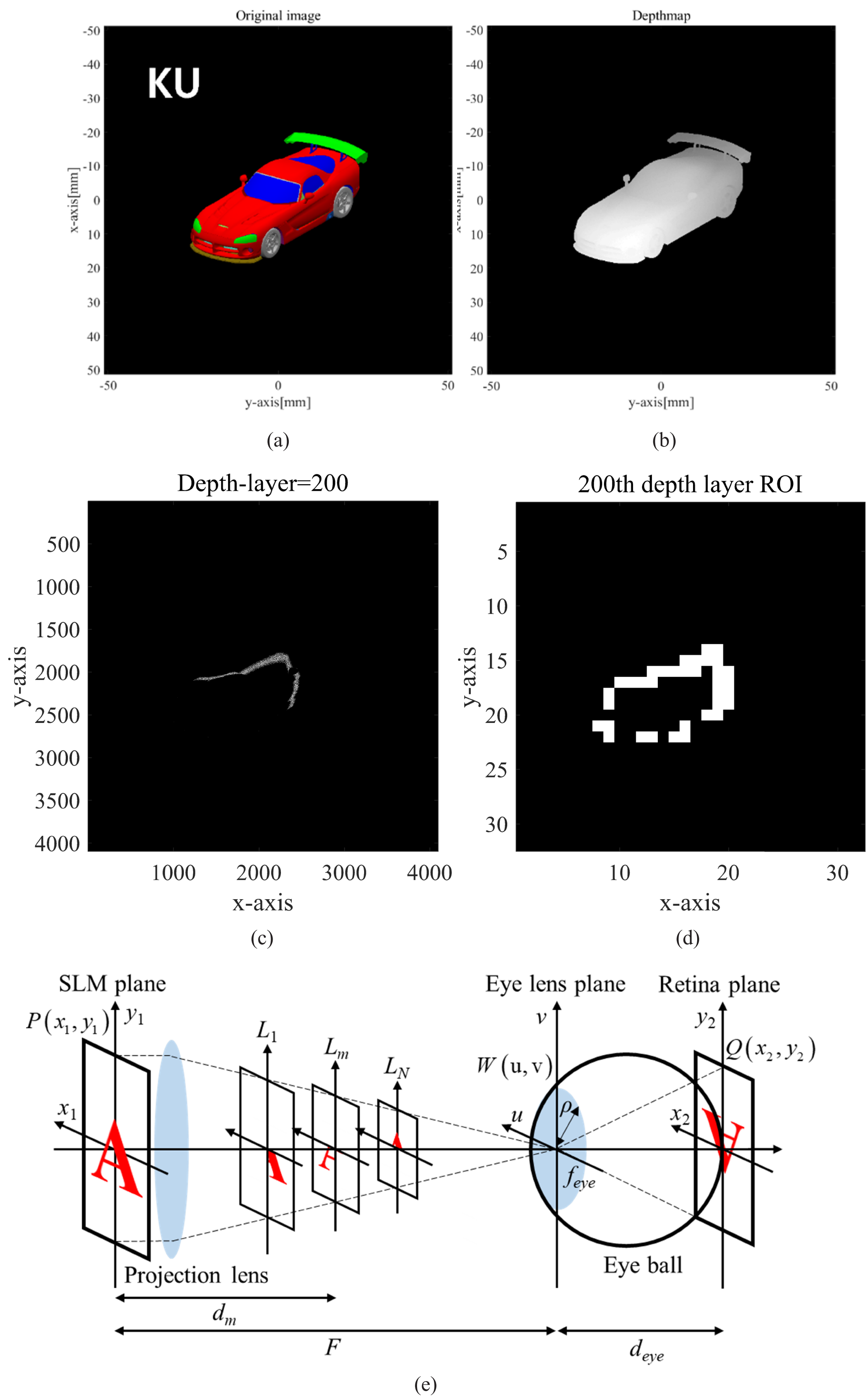

FIG. 1. Scheme of a layer-based creating computer-generated holograms (CGH): (a) original intensity data, (b) depth-information data, (c) data of the 200th depth layer, (d) region of interest (ROI) of the 200th depth layer, and (e) conventional CGH calculation method. The CGH size is set to 4096 × 4096 with the sampling interval $\Delta x = \Delta y = 58.05$ μm, 256 depth levels, and partition number 32 × 32.

scene in the free space is represented by the cumulatively superposed CGH pattern. Computationally, the FFT is used twice in the ICdFr: first in the transform from the retina plane (x_2, y_2) to the eye-lens plane (u, v), and second in the transform from the eye-lens plane to the SLM plane (x_1, y_1) (See Appendix). The conventional ICdFr algorithm is inefficient, since a full-resolution ICdFr should be carried out at each depth layer. Regardless of the sparsity of the depth image, the application of ICdFr (which applies to every depth layer) via double full-resolution FFTs can be inefficient. The sparsity of the layered 3D scene was noted in a few previous works. In refs. [10–13], the subsparse 2D-FFT algorithm was designed to exclude zero columns and zero rows in the FFT computation, to speed up the conversion of the layered 3D image to CGH by exploiting the areal sparsity in the layered model of a 3D scene. This method was limited, however, in that it could only partially squeeze the zero-valued dummy area in the 2D FFT form. In this paper, we propose a sparsity-driven field-localization-based fast algorithm for layered CGHs, featuring full-squeezing of zero values and parallelization of local FFTs.

II. SPARSE-FIELD-LOCALIZATION METHOD

A larger localized region that covers the nonzero-valued region of the layer is specified, and referred to as the region of interest (ROI) [Fig. 1(d)]. The whole area is partitioned into 32 × 32 local partition areas, and the local region covering the specific depth image forms the ROI mask. Figure 2(a) schematically presents the main idea of the proposed field-localization concept. Considering a localized piece of image at the layer L_m [Fig. 1(d) and Fig. 2(a)], the ROI indicated by the solid rectangle is set to cover the nonzero-valued area in the depth plane L_m. This corresponds to a localized area in the retina plane, as illustrated in Fig. 2(a). The expectation is that the local rectangular ROI at depth plane L_m can be transformed to the corresponding local part in the SLM plane, and that the reduced-size ICdFr can be used for this purpose. For instance, the computational domain of resolution $M \times N$ is divided into $m \times n$ rectangular pieces of resolution $(M / m) \times (N / n)$. In the conventional computation scheme [Fig. 1(e)], the 2D-FFT calculation processes the $M \times N$ image as a whole. However, the proposed method [Fig. 2(b)] divides the total resolution by $m \times n$, and then performs the 2D-FFT calculation on each piece. Performing this fragmentation generates a significant gain in terms of the operational complexity of the 2D-FFT calculation. Generally, when a 2D-FFT calculation is performed on an image with a resolution of $M \times N$, the computational complexity is $O[2MN \log(MN)]$. However, if the field-localization method is used to divide the image of $M \times N$ resolution into $m \times n$ pieces, the complexity becomes $O[2MN (\log(MN) - \log(mn))]$.

In addition, the proposed method is able to squeeze the zero-valued dummy region maximally, and thereby optimize CGH-calculation performance. Let us denote the total number of local subpatches as w_H, which is obviously smaller than $m \cdot n \cdot H$. Let the set of ROI be then defined by

$$R=\left\{I_1,\cdots,I_{w_H}\right\}=R_1\cup R_2\cup R_3\cdots R_{H-1}\cup R_H, \tag{1}$$

where the sub-ROIs are defined by

$$\begin{aligned}&R_1=\left\{I_1,\cdots,I_{w_1}\right\},\ R_2=\left\{I_{w_1+1},\cdots,I_{w_2}\right\},\ \cdots,\\&R_k=\left\{I_{w_k+1},\cdots,I_{w_{k+1}}\right\},\ R_H=\left\{I_{w_{H-1}+1},\cdots,I_{w_H}\right\}.\end{aligned} \tag{2}$$

When the h^{th} depth is empty, meaning that $R_h = \{I_{w_{h-1}+1}, ..., I_{w_h}\} = \phi$, then we can set $w_{h-1} = w_h$. Thus the localized empty segments that do not require calculation can be filtered. As a result, the calculation of the black area that occupies most of Fig. 1(d) can be skipped, greatly reducing the computation required.

The field-localized-based CGH synthesis method can be described as follows: $Q(x_2, y_2)$ of the retina plane and $P(x_1, y_1)$ of the SLM plane have a mathematical relationship, represented by

$$Q(x_2,y_2)=CdFr\left\{P(x_1,y_1);F,d_{eye},f_{eye},\rho\right\}, \tag{3}$$

$$P(x_1,y_1)=ICdFr\left\{Q(x_2,y_2);F,d_{eye},f_{eye}\right\}, \tag{4}$$

where CdFr is a cascaded Fresnel transform, F is the focal length of the projection lens, d_{eye} is the distance between the eye-lens plane and the retina plane, f_{eye} is the focal length of the eye lens, and p is the pupil size. The relationship between one piece $Q'(x_2, y_2)$, $P'(x_1, y_1)$ and the entire image $Q(x_2, y_2)$, $P(x_1, y_1)$, which is fragmented by the field-localization method, can be expressed as

$$Q(x_2,y_2)=\sum_{k=1}^{m}\sum_{l=1}^{n}Q'_{kl}\left(x_2-\bar{x}_{2,k},y_2-\bar{y}_{2,l}\right), \tag{5}$$

$$P(x_1,y_1)=\sum_{k=1}^{m}\sum_{l=1}^{n}P'_{kl}\left(x_1-\bar{x}_{1,k},y_1-\bar{y}_{1,l}\right), \tag{6}$$

where k and l are the segmentation numbers of the x- and y-axis directions respectively.

The centers of the local patches at the x_1, y_1 and x_2, y_2 planes are related by $(\bar{x}_{2,k},\bar{y}_{2,l})=(\bar{x}_{1,k},\bar{y}_{1,l})$. A piece $Q'(x_2, y_2)$ of the retina plane and a piece $P'(x_1, y_1)$ of the SLM plane are likewise expressed as

$$Q'(x_2,y_2)=CdFr\left\{P'(x_1,y_1);F,d_{eye},f_{eye},\rho\right\}, \tag{7}$$

$$P'(x_1,y_1)=ICdFr\left\{Q'(x_2,y_2);F,d_{eye},f_{eye}\right\}. \tag{8}$$

The partition number $m \times n$ is a crucial parameter, and its value should be optimized for parallel acceleration. Figure 3 shows a comparison of the CGH formed with different partition numbers, 8 × 8 and 32 × 32, based on the observed images in the retina plane. In the images in Figs. 3(a) and 3(b), crossed-grid patterns of line defects are ap-

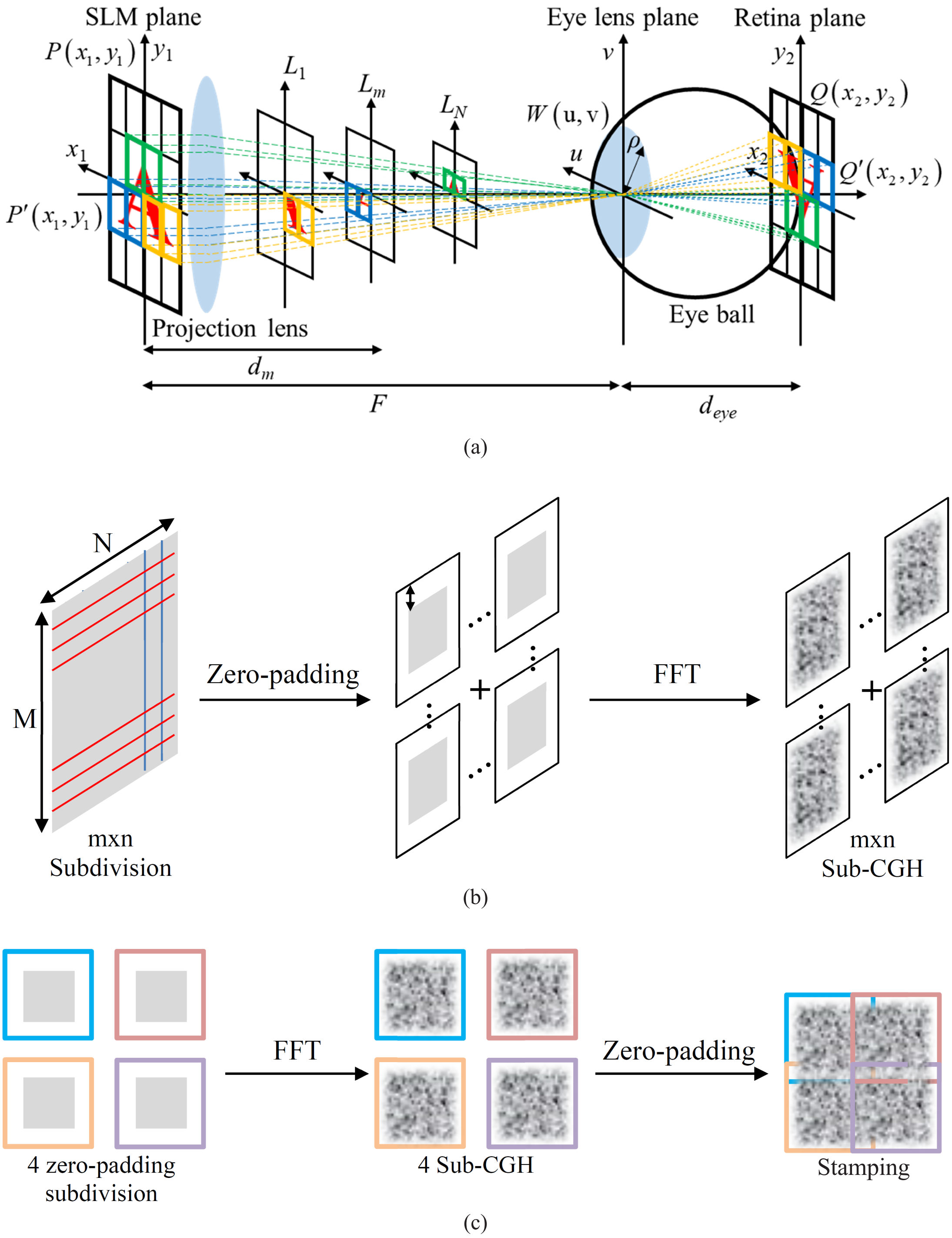

FIG. 2. The proposed creating computer-generated holograms (CGHs) calculation scheme: (a) schematics of the proposed field-localization-based CGH synthesis method, (b) CGH calculation process, and (c) zero-padding and stamping techniques.

parent. Such a defect pattern is caused by the cut-off effect of the edge diffraction of each rectangular partition, and occurs regardless of the partition number, which means the necessary edge-diffraction field is not accounted for by the simple partitioning scheme presented in Fig. 2(a).

This defect problem can be resolved by surrounding the corresponding subsection in the retina plane with a rectangular zero-padding region, as shown in Figs. 2(b) and 2(c). Figure 4 presents a comparison of the 32 × 32-partitioned CGH without and with the zero-padding region, by observation in the retina plane. In Figs. 4(a) and 4(b), the sub-CGH images without and with the zero padding are compared, to clarify the effect of the zero-padding region.

Let $S_{m,min}$ be the size of a local patch with zero padding. The range of the ROI should be expanded to account for edge diffraction, which is affected by the distance between

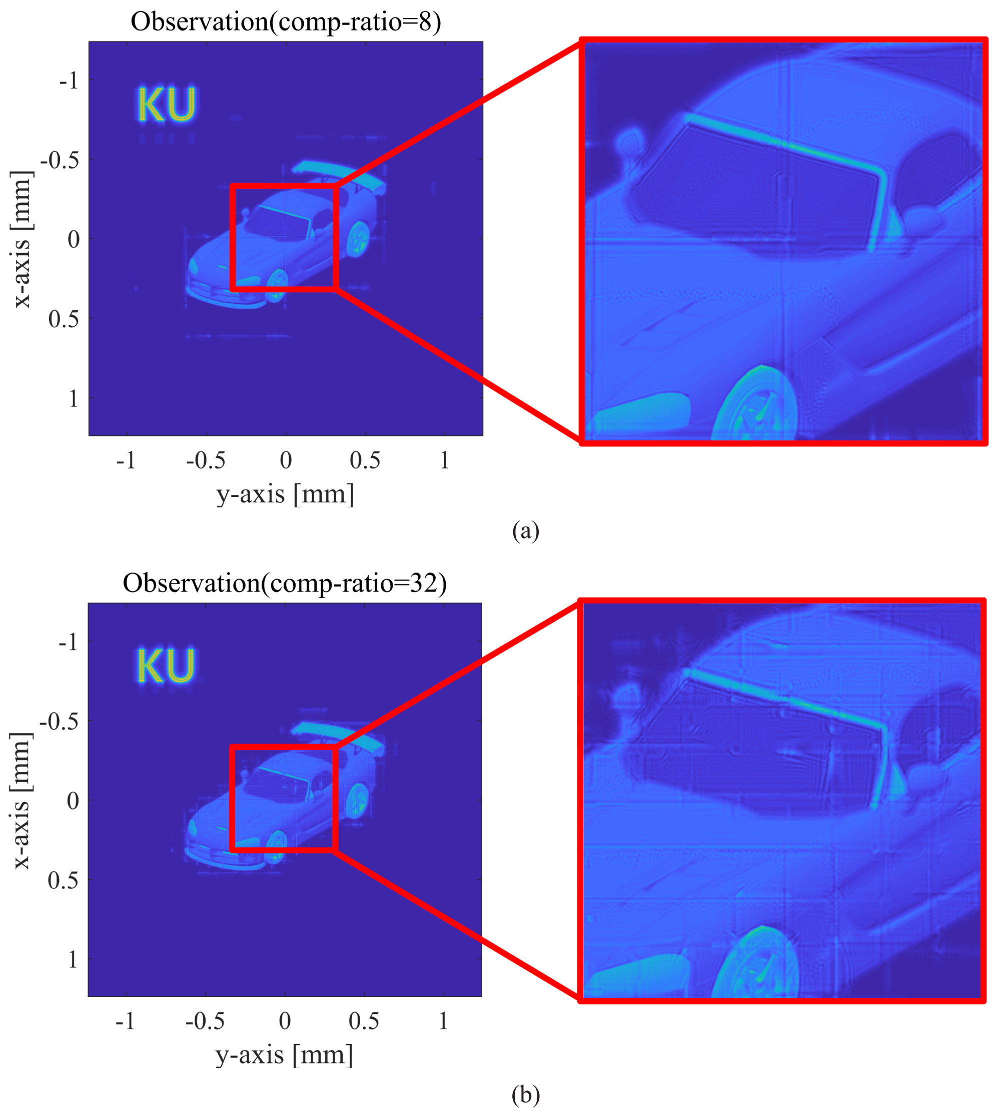

FIG. 3. Observation images for different partition numbers: (a) 8 × 8 field-localization result, and (b) 32 × 32 field-localization result. Here the parameters of the simulation are given as the resolution = 4096 × 4096, pixel pitch = 58.05 μm, depth level = 8, $d_1 = F = 2.4$ m, $d_2 = 25$ mm, and max distance = 1.5 m.

the SLM and the depth plane. Therefore, the required size of zero padding varies, depending on the distance of the depth plane. The required ROI size can be derived from the Nyquist sampling criteria for the instantaneous spatial frequency as

$$S_{\mathrm{m,min}} = \left|\frac{2}{\lambda}\left(\frac{1}{F} - \frac{1}{F-d_m}\right)\right| \frac{\lambda^2 F^2}{\Delta x_1}\eta + \frac{\lambda F}{\pi}\omega_{sig,\max} < S_m, \quad (9)$$

where S_m is the local patch size at the CGH plane, and η and $u_{\max}$ are $\eta = r_{eye} / u_{\max}$ and $u_{\max} = \lambda d_1 / (2\Delta x_1)$ respectively. In Fig. 2(a) the focal length of the eye f_{eye} is tuned to the layer d_m, so the wavefront of the optical field just after passing the eye lens is represented by $e^{j\frac{\pi}{\lambda}\left(1/F+1/d_{eye}-1/f_{eye}\right)\left(u^2+v^2\right)} = e^{j\frac{\pi}{\lambda}\left(1/F-1/(F-d_m)\right)\left(u^2+v^2\right)}$ [5, 8]. Let $\omega_{sig,\max}$ be the maximum bandwidth of the CGH signal field; then the Nyquist sampling criteria for instantaneous spatial frequency is given by

$$\left|\frac{\partial\phi}{\partial u}\right|_{u=\eta\cdot u_{\max}} = \left(\left|\frac{2\pi}{\lambda}\left(\frac{1}{F} - \frac{1}{F-d_m}\right)\right| u_{\max}\eta\right) + \omega_{sig,\max} < \frac{2\pi}{2\Delta u}. \quad (10)$$

By substituting $u_{\max} = \lambda d_1 / (2\Delta x_1)$ into Eq. (10), Eq. (9) can be obtained. However, in practice the appropriate zero-padding size that removes the crossed-grid line defect can be determined by simulation-based adjustment.

The sub-CGH pattern is perfectly expressed on the extended subregion in the CGH plane, and the total accumulation of the sub-CGH pattern is equivalent to the conventional CGH pattern, as presented in Fig. 4(b). Simply

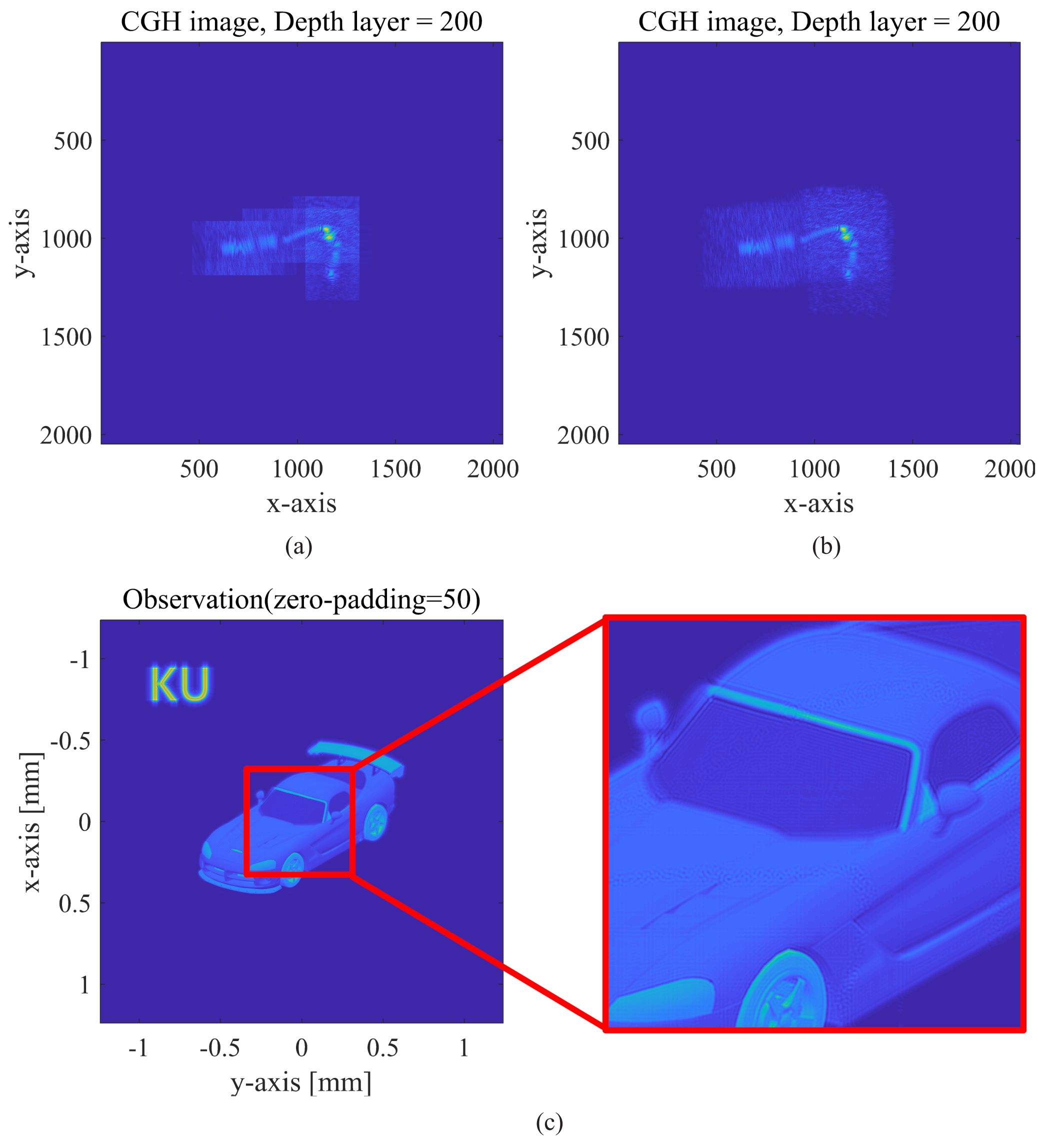

FIG. 4. Observation of the zero-padding effect on the creating computer-generated holograms (CGHs) image: (a) sub-CGH pattern without zeropadding at the 200th depth layer, (b) sub-CGH pattern with zero padding at the same layer, and (c) CGH image observed at the retina plane with a zero-padding size of 70 pixels. The simulation parameters are set as the resolution = 4096 ×4096, pixel pitch = 58.05 μm, depth level = 256, partition number = 32 × 32, $d_1 = F = 2.4$ m, $d_2 = 25$ mm, and max distance = 1.5 m.

changing the zero padding reveals that the quality of the resulting CGH image gradually improves with zero-padding thickness. In fact, under the given conditions, differences between the resultant image and one produced by the conventional method are hard to find when using a zero-padding size of more than 70 pixels. The CGH image with 70-pixel zero padding is shown in Fig. 4(c).

III. SIMULATION RESULTS

Figure 5 simulates the observation results of CGH by the conventional method and the proposed method. The results were observed by simulation of CGH generated at depth 256, focusing on depth 0 and depth 245. It has focus on the "KU" word in the background, where the depth is 0, and on the front light of the car, where the depth is 245. Visually comparing Fig. 5(a), 5(c) and Fig. 5(b), 5(d), almost same results are acquired. However, the calculation times for the two methods are significantly different.

Figure 6 compares the computation time of CGHs by the depth-layer numbers, using the conventional and proposed methods under the same geometric conditions. The 3D model object is a car, as shown in Fig. 5. The calculation times differ significantly, even at eight depth levels: The first global-calculation time is 22.7158 seconds while the local-calculation time is 2.1167 seconds, so the latter computational efficiency is about 10 times as good, under the test conditions. The difference in computation times diverges

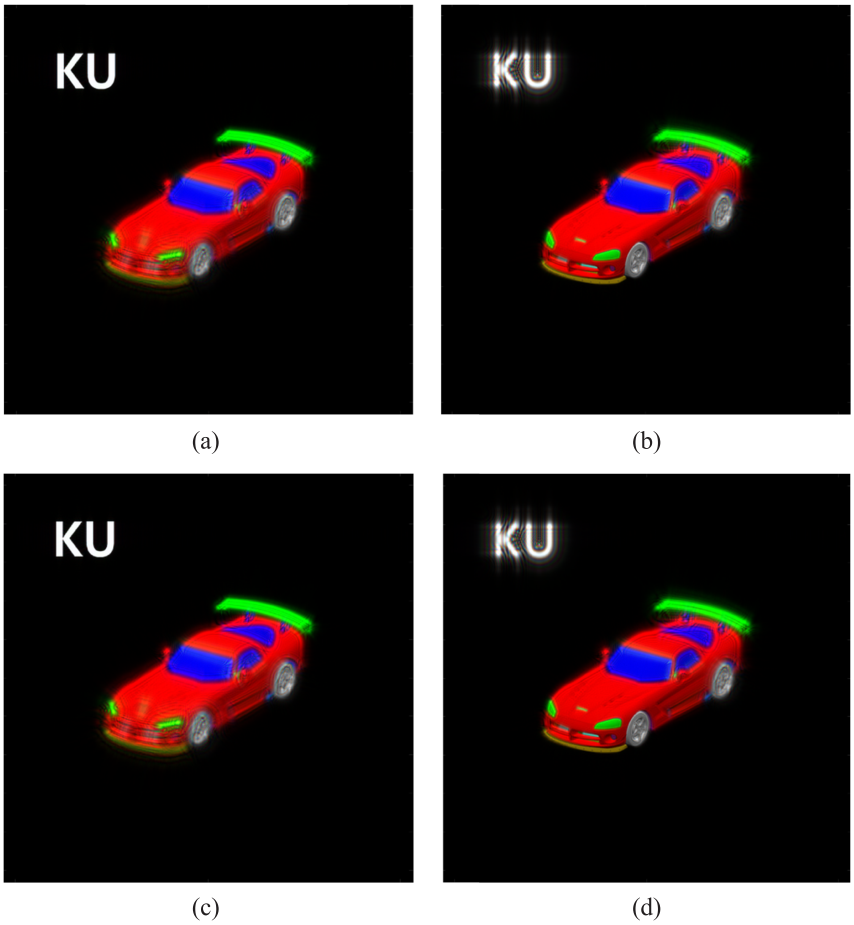

FIG. 5. Full-color creating computer-generated holograms (CGHs) observation results focused on (a) depth of 0 and (b) depth of 245 for the conventional method, and (c) depth of 0 and (d) depth of 245 for the proposed method. The parameters of the simulation are the resolution = 4096, pixel pitch = 25 μm, partition number = 32 × 32, d_1 = 2.4 m, d_2 = 25 mm, max distance = 1.5 m, and depth level = 256.

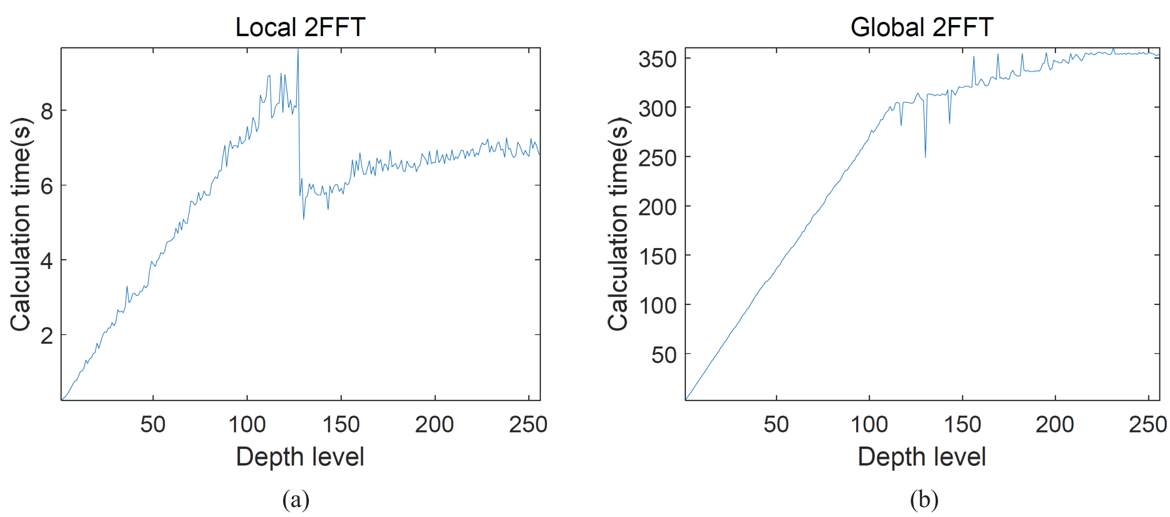

FIG. 6. Calculation time for (a) the local algorithm and (b) the global algorithm, by depth level. The parameters of the simulation are the resolution = 4096 × 4096, pixel pitch = 25 μm, partition number = 32 × 32, d_1 = 2.4 m, d_2 = 25 mm, max distance = 1.5 m, and depth level = 256.

further as the depth level of the 3D scene increases. Figure 6(b) shows a linear increase in calculation time with depth level, while Fig. 6(a) shows that the computation time does not increase considerably with depth level. This is because the computation applied to the set of ROI of Eq. (1) does not significantly increase with depth level, meaning that the enhancement in computational efficiency increases with models of higher depth level. In Fig. 6, the rate of change of computation time with depth level suddenly shifts at a depth level of about 128. This occurs sometimes when the 3D model can be approximated less by the axially nonuniform multi-levels than by the axially regular uniform depth levels. Proper representation of the 3D model requires an optimal depth level, and even axially nonuniform model layering. In this example simulation, we find that the 3D model requires a depth level of 128 when we use uniform model layering.

The proposed field-localization algorithm is advantageous for parallel computation, because divided multiple ROI fields can be calculated parallelly in each depth layer, as shown in Eq. (2). This complexity reduction greatly improves the efficiency of CGH computation. On the other hand, the conventional method can perform parallel operations only in units of depth layers, so there is a limit to the efficiency of parallel computation.

IV. CONCLUSION

In conclusion, we have proposed a fast layer-based CGH algorithm that enables efficient parallel computation. The design elements of the fast layer-based CGH algorithm to ensure CGH quality equivalent to that of the conventional algorithm were presented, and the results were compared and analyzed by simulation.

APPENDIX

1. Representations of CdFR and ICdFR

The generalized cascaded Fresnel transform (CdFr) is represented by (see Fig. 1(e))

$$\begin{aligned} Q(x_2, y_2) &= \mathrm{CdFr}\{P(x_1, y_1); F, d_2, f, \rho\} \\ &= \frac{1}{(j\lambda d_1)(j\lambda d_2)} e^{j\frac{\pi}{\lambda d_2}(x_2^2+y_2^2)} \iint \left[e^{j\frac{\pi}{\lambda}\left(\frac{1}{d_1}+\frac{1}{d_2}-\frac{1}{f}\right)(u^2+v^2)} circ\left(\frac{u^2+v^2}{\rho^2}\right)\right) \\ &\times \iint e^{j\frac{\pi}{\lambda}\left(\frac{1}{d_1}-\frac{1}{F}\right)(x_1^2+y_1^2)} P(x_1, y_1) e^{-j\frac{2\pi}{\lambda d_1}(x_1 u + y_1 v)} dx_1 dy_1 \Bigg] e^{-j\frac{2\pi}{\lambda d_2}(u x_2 + v y_2)} du dv. \end{aligned} \tag{A1}$$

The inverse generalized cascaded Fresnel transform (ICdFr) is represented by

$$\begin{aligned} P(x_1, y_1) &= \mathrm{ICdFr}\{Q(x_2, y_2); F, d_2, f\} = e^{\left(j\frac{\pi}{\lambda F}(x_1^2+y_1^2)\right)} P'(x_1, y_1) \\ &= e^{\left(j\frac{\pi}{\lambda F}(x_1^2+y_1^2)\right)} \left(\frac{j}{\lambda d_1}\right)\left(\frac{j}{\lambda d_2}\right) e^{-j\frac{\pi}{\lambda d_1}(x_1^2+y_1^2)} \iint e^{-j\frac{\pi}{\lambda}\left(\frac{1}{d_1}+\frac{1}{d_2}-\frac{1}{f}\right)(u^2+v^2)} \\ &\left[\iint e^{-j\frac{\pi}{\lambda d_2}(x_2^2+y_2^2)} Q(x_2, y_2) e^{j\frac{2\pi}{\lambda d_2}(x_2 u + y_2 v)} dx_2 dy_2\right] e^{j\frac{2\pi}{\lambda d_1}(x_1 u + y_1 v)} du dv \\ &= \left(\frac{j}{\lambda d_1}\right)\left(\frac{j}{\lambda d_2}\right) e^{\left(-j\frac{\pi}{\lambda}\left(-\frac{1}{F}+\frac{1}{d_1}\right)(x_1^2+y_1^2)\right)} \iint e^{-j\frac{\pi}{\lambda}\left(\frac{1}{d_1}+\frac{1}{d_2}-\frac{1}{f}\right)(u^2+v^2)} \\ &\left[\iint e^{-j\frac{\pi}{\lambda d_2}(x_2^2+y_2^2)} Q(x_2, y_2) e^{j\frac{2\pi}{\lambda d_2}(x_2 u + y_2 v)} dx_2 dy_2\right] e^{j\frac{2\pi}{\lambda d_1}(x_1 u + y_1 v)} du dv. \end{aligned} \tag{A2}$$

ACKNOWLEDGMENT

This work was supported by Samsung Research Funding & Incubation Center of Samsung Electronics under Project Number SRFC-TB1903-05.

REFERENCES

1. Y.-L. Piao, M.-U. Erdenebat, K.-C. Kwon, S.-K. Gil, and N. Kim, "Chromatic-dispersion-corrected full-color holographic display using directional-view image scaling method," Appl. Opt. **58**, A120–A127 (2019).
2. Y. Zhao, M.-U. Erdenebat, M.-S. Alam, M.-L. Piao, S.-H. Jeon, and N. Kim, "Multiple-camera holographic system featuring efficient depth grids for representation of real 3D objects," Appl. Opt. **58**, A242–A250 (2019).
3. R. H.-Y. Chen and T. D. Wilkinson, "Computer generated hologram from point cloud using graphics processor," Appl. Opt. **48**, 6841–6850 (2009).
4. T. Senoh, K. Yamamoto, R. Oi, T. Mishina, and M. Okui, "Computer generated electronic holography of natural scene from 2D multi-view images and depth map," in Proc. *2008 Second International Symposium on Universal Communication* (Osaka, Japan, Dec. 2008), pp. 126–133.
5. J. Roh, K. Kim, E. Moon, S. Kim, B. Yang, J. Hahn, and H. Kim, "Full-color holographic projection display system featuring an achromatic Fourier filter," Opt. Express **25**, 14774–14782 (2017).
6. J.-H. Park and M. Askari, "Non-hogel-based computer generated hologram from light field using complex field recovery technique from Wigner distribution function," Opt. Express **27**, 2562–2574 (2019).
7. D. Im, J. Cho, J. Hahn, B. Lee, and H. Kim, "Accelerated synthesis algorithm of polygon computer-generated holograms," Opt. Express **23**, 2863–2871 (2015).
8. D. Im, E. Moon, Y. Park, D. Lee, J. Hahn, and H. Kim, "Phase-regularized polygon computer-generated holograms," Opt. Lett. **39**, 3642–2645 (2014).
9. A. Symeonidou, D. Blinder, A. Munteanu, and P. Schelkens, "Computer-generated holograms by multiple wavefront recording plane method with occlusion culling," Opt. Express **23**, 22149–22161 (2015).
10. P. Su, W. Cao, J. Ma, B. Cheng, X. Liang, L. Cao, and G. Jin, "Fast computer-generated hologram generation method for three-dimensional point cloud model," J. Display Technol. **12**, 1688–1694 (2016).
11. J. Jia, J. Si, and D. Chu, "Fast two-step layer-based method for computer generated hologram using sub-sparse 2D fast Fourier transform," Opt. Express **26**, 17487–17497 (2018).
12. H. G. Kim, H. Jeong, and Y. M. Ro, "Acceleration of the calculation speed of computer-generated holograms using the sparsity of the holographic fringe pattern for a 3D object," Opt. Express **24**, 25317–25328 (2016).
13. H. Kim and Y. Ro, "Ultrafast layer based computer-generated hologram calculation with sparse template holographic fringe pattern for 3-D object," Opt. Express **25**, 30418–30427 (2017).